Materials Science in Semiconductor Processing 198 (2025) 109755

Contents lists available at ScienceDirect

Materials Science in Semiconductor Processing

journal homepage: www.elsevier.com/locate/mssp

High-performance NIR reflective yellow pigment for sustainable cool surface coatings to address urban heat island mitigation

A. Mridula [a,b], M. Rakshita [a], K.A.K. Durga Prasad [a], Subrata Das [c], K. Uday Kumar [a,*], S. Surendra Babu [b], R. Rakesh Kumar [a], D. Haranath [a,**]

[a] Energy Materials and Devices Group, Department of Physics, National Institute of Technology Warangal, Hanumakonda, Telangana, India, 506004
[b] Directorate of Laser Systems, Research Center Imarat, Hyderabad, India, 500069
[c] Materials Science and Technology Division, CSIR-National Institute for Interdisciplinary Science and Technology, Thiruvananthapuram, Kerala, India, 695019

ARTICLE INFO

Keywords:
NIR reflectance
Yttrium phosphate
Cool pigments
Urban heat island

ABSTRACT

A novel, environmentally friendly, near-infrared (NIR) solar reflective yellow pigment has been successfully developed by incorporating bismuth (Bi^{3+}) and vanadium (V^{5+}) into the yttrium phosphate (YPO_4) host lattice. $Y_{(1-x)}Bi_xP_{(1-y)}V_yO_4$ (x = y = 0–1) materials with different composition were synthesized using two distinct approaches: the flux-assisted solid-state method (SSM) and the co-precipitation technique (CPS), and the results were compared. A drastic shift in the absorption curve towards higher wavelengths is observed for the materials synthesized by the solid-state reaction method and co-precipitation at 900 °C. Secondary phases were noticed in both methods of preparation due to the high ionic radii of the dopant ions. Notably, the simultaneous incorporation of Bi^{3+} and V^{5+} significantly enhanced both the NIR solar reflectance and the intensity of the yellow color in the synthesized materials. The co-doping effect induced a well-defined morphology, improving the light-scattering efficiency and boosting the NIR solar reflectance. The optimized composition, $Y_{0.4}Bi_{0.6}P_{0.4}V_{0.6}O_4$, achieved a high reflectance value of 54.64%, compared to just 38% for the undoped host. With a vivid yellow body color, high solar reflectance (54.64 %), and excellent stability, $Y_{0.4}Bi_{0.6}P_{0.4}V_{0.6}O_4$ emerges as a promising, sustainable alternative for cool yellow pigments in energy-efficient coatings and architectural applications.

1. Introduction

The urban heat island (UHI) effect is a major environmental concern, causing urban areas to retain more heat than their rural surroundings. This results from prolonged absorption of solar radiation by buildings and infrastructure during the day, coupled with inadequate heat dissipation at night [1]. The temperature disparity between urban and rural regions is exacerbated by the lack of natural greenery in cities, which otherwise facilitates rapid radiative cooling. To mitigate excessive indoor temperatures, air conditioning is widely used, consuming nearly 40 % of total electricity. Heat absorption is particularly high in buildings made of asphalt, cement, concrete, and metal structures [2]. Given that approximately 53 % of solar radiation falls within the near-infrared (NIR) spectrum, coatings with NIR-solar reflective materials can significantly lower indoor temperatures, earning them the designation of "cool coating materials [3]."

Recent research has focused on rare-earth-based NIR-solar reflective pigments to enhance reflectivity while preserving aesthetic appeal. For instance, doping Eu^{3+}/Sr^{2+} and Mg^{2+} in $SrCuSi_4O_{10}$ altered its sky-blue hue to dark blue, significantly boosting NIR reflectance with a 20 % dopant substitution [4,5]. Similarly, green pigments $(Y_{1-x}R_x)_2Cu_2O_5$ (R= In; Sc; Lu) synthesized via solid-state reactions offer an eco-friendly alternative to toxic Cr and Co-based pigments [6]. Yellow pigment research has also made advancements. Vanadium-based pigments have garnered attention for producing yellow hues from originally white materials. The pentavalent V^{5+} state in V_2O_5 exhibits yellow coloration due to charge transfer transitions ($O^{2-} \rightarrow V^{5+}$). V-$ZrO_2$, synthesized through various methods, confirms V incorporation into ZrO_2, inducing a yellow tint [7,8]. Gopal et al. observed an unusual optical shift in V^{5+} substituted BPO_4, transforming its open-framework white structure into yellow phosphovanadate. Additionally, $BiVO_4$ has emerged as a promising industrial yellow pigment. Overall, the strategic substitution or

This article is part of a special issue entitled: Energy & Sensing published in Materials Science in Semiconductor Processing.

* Corresponding author.
** Corresponding author.
E-mail addresses: kanapuram.udaykumar@nitw.ac.in (K.U. Kumar), haranath@nitw.ac.in (D. Haranath).

https://doi.org/10.1016/j.mssp.2025.109755
Received 14 May 2025; Received in revised form 30 May 2025; Accepted 3 June 2025
Available online 6 June 2025

doping of bismuth and vanadium ions presents a viable path toward the development of eco-friendly yellow pigments [9].

Lanthanide-based orthophosphates ($LnPO_4$) have recently emerged as a crucial class of inorganic materials with diverse applications, including laser hosts, phosphors, photon up-conversion, and bio-imaging [10]. These phosphates exist in multiple polymorphic forms -monoclinic monazite, tetragonal xenotime, tetragonal zircon, monoclinic churchite, and hexagonal rhabdophane—determined by the synthesis method and the nature of the metal cation [11,12]. Key rare-earth phosphates in this category include $CePO_4$, $PrPO_4$, YPO_4, $LuPO_4$, $LaPO_4$, $GaPO_4$, and $EuPO_4$. Their physical, chemical, and optical properties can be tailored through selective doping[13–15].

Among them, yttrium phosphate (YPO_4) is particularly significant due to its high chemical stability and versatile applications. It crystallizes in two distinct structures: hexagonal (D_2 symmetry) and tetragonal (D_{2d} symmetry), the latter existing as xenotime ($I4_1/amd$ space group), where Y^{3+} follows D_{2d} symmetry. YPO_4 comprises chains of corner-shared YO_8 dodecahedra and PO_4 tetrahedra, making it an excellent luminescent host with high quantum efficiency and well-defined absorption and emission spectra. Its strong UV absorption and vacuum stability makes it a promising red-emissive material for display technologies, including plasma displays [14].

Eu^{3+}-doped YPO_4 has been widely studied for red light emission. Additionally, YPO_4's high thermal expansion coefficient enables its use as a green barrier coating for silicon ceramics [16]. Ce^{3+}/Tb^{3+} co-doped YPO_4 has shown potential as a WLED glass ceramic material due to its enhanced luminescence [17,18]. Similarly, Dy^{3+}: YPO_4 and Sm^{3+}: YPO_4 co-doped with Bi^{3+} exhibit superior emission properties [19]. Given that the optical and physical properties of YPO_4 are highly synthesis-dependent, selecting an optimal preparation method is critical for achieving precise size, morphology, and crystallinity [14,20].

Water-based synthesis routes are preferred over organic solvent-based methods due to their environmental safety. Various approaches, including solid-state reactions, precipitation, hydrothermal, solvothermal, and ion-exchange methods, have been explored to synthesize micro- and nanostructured YPO_4 [14,16,19]. Among these, the chemical co-precipitation method is particularly advantageous due to its high purity, scalability, reproducibility, minimal solvent usage, and cost-effectiveness. In this process, metal precursors are precipitated as hydroxides using agents such as NH_4OH, NaOH, or tetramethylammonium hydroxide, followed by calcination [21].

While YPO_4 has been extensively studied for luminescence, its potential as an NIR-reflective pigment remains unexplored. In this study, we investigate the NIR-reflective and color properties of YPO_4 and its bismuth- and vanadium-substituted derivatives, synthesized via a simple precipitation method, demonstrating their suitability for cool coating applications.

2. Materials and methods

2.1. Materials

Yttrium oxide (99 %), bismuth oxide (98 %), diammonium phosphate (98 %), ammonium metavanadate (98 %), and yttrium (III) nitrate hexahydrate (98 %) were used as precursors. All chemicals were procured from SRL Private Limited, India, and used without further purification.

2.2. Method of synthesis

Materials with the composition $Y_{(1-x)}Bi_xP_{(1-y)}V_yO_4$ (x = y = 0.6) were synthesized using both solid-state reaction (SSM) and co-precipitation methods (CPS). For the solid-state reaction method, yttrium oxide, bismuth oxide, diammonium phosphate, and vanadium pentoxide were thoroughly ground for 2 h to ensure homogeneous mixing. The mixture was then packed into a recrystallized alumina crucible and calcined at 900 °C in air using a muffle furnace for 3 h (shown in Fig. 1a). For the co-precipitation method, bismuth nitrate was first prepared by dissolving bismuth oxide (Bi_2O_3) with nitric acid (HNO_3) through a dropwise addition, resulting in the dissolution of the oxide. This dissolution indicates the conversion of bismuth oxide to bismuth nitrate ($Bi(NO_3)_3$), and the reaction is shown below. $Bi_2O_3 + 6HNO_3 \rightarrow 2Bi(NO_3)_3 + 3H_2O$. This solution was then mixed with yttrium nitrate solution, followed by the dropwise addition of diammonium phosphate solution under continuous stirring for 90 min. Ammonium metavanadate, pre-dissolved in DI water, was then added to the above solution (pH is 2) and further ammonia solution is added until the pH was adjusted to 4. The resulting precipitate was collected via centrifugation, washed sequentially with DI water and ethanol, dried at 100 °C for 3 h, and finally calcined at 900 °C for 90 min (shown in Fig. 1b).

2.3. Characterization techniques

Powder X-ray diffraction (XRD) was used to confirm the phase formation of the synthesized powder materials. Structural analysis was performed using a Bruker D8 Advance diffractometer with Cu Kα radiation (λ = 1.54056 Å) at a scan rate of 0.01 s^{-1}. Fourier Transform Infrared Spectroscopy (FTIR) was employed to identify functional groups and characterize stretching and bending vibrations in the 400–4000 cm^{-1} range using a Bruker Alpha-II instrument. Surface morphology and elemental composition were analyzed using a Zeiss Scanning Electron Microscope (SEM). Absorbance and diffuse reflectance spectra were recorded with a Shimadzu UV-3600 Plus spectrophotometer in the 200–1600 nm range with a step size of 1 nm. Thermogravimetric analysis (TGA) was conducted using a PerkinElmer TGA instrument in a flowing air atmosphere at a heating rate of 10 °C/min. Quantum efficiency was measured using an Enlitech system (300–1100 nm) equipped with an integrating sphere and $BaSO_4$ as the standard. Excitation and emission spectra were recorded with a Hitachi F-4700 fluorescence spectrophotometer. Near-infrared (NIR) reflectance (R*) of the synthesized materials was determined using a Shimadzu UV-3600 UV–Vis–NIR spectrophotometer based on a standard calculation formula, which is in accordance with ASTM standard G159-99.

3. Results and discussion

3.1. Powder XRD (PXRD) analysis

The powder X-ray diffraction (PXRD) technique was utilized to determine the crystal structure, phase purity, lattice parameters, and average crystallite size of the synthesized materials. Fig. 2 represents the PXRD pattern of $Y_{(1-x)}Bi_xP_{(1-y)}V_yO_4$ (x = y = 0.6). The diffraction peaks observed at specific 2θ angles correspond well with the standard tetragonal zircon-type structure (JCPDS No. 74–2429), which crystallizes in the $I4_1/amd$ space group [22,23]. Calculated lattice parameters are a = b = 6.913 nm and c = 6.174 nm, with an average crystallite size of 98 nm. The presence of secondary phases, primarily $BiPO_4$, was identified in the YPBV-SSM, YPBV-CPS@900 °C, and YPBV-CPS@100 °C materials. This phase formation is attributed to the high Bi^{3+} substitution level (x = 0.6), which induces structural instability, leading to phase segregation in the $Y_{0.4}Bi_{0.6}P_{0.4}V_{0.6}O_4$ system. The incorporation of Bi^{3+} (ionic radius, r = 1.03 Å) into the smaller Y^{3+} lattice (r = 0.9 Å) results in lattice expansion, leading to the emergence of $BiPO_4$ as a secondary phase in all three materials. Additionally, the substitution of V^{5+} (r = 0.36 Å) into the P^{5+} (r = 0.17 Å) lattice induces a noticeable shift in the diffraction peaks toward lower angles, confirming the formation of a tetragonal structure. This shift arises due to the increased lattice strain, as the smaller P^{5+} ions, with a coordination number of 4, struggle to accommodate the larger V^{5+} ions. As a consequence, the induced structural distortion leads to the observed peak shift in the PXRD pattern.

Similar observations have been reported in the literature concerning

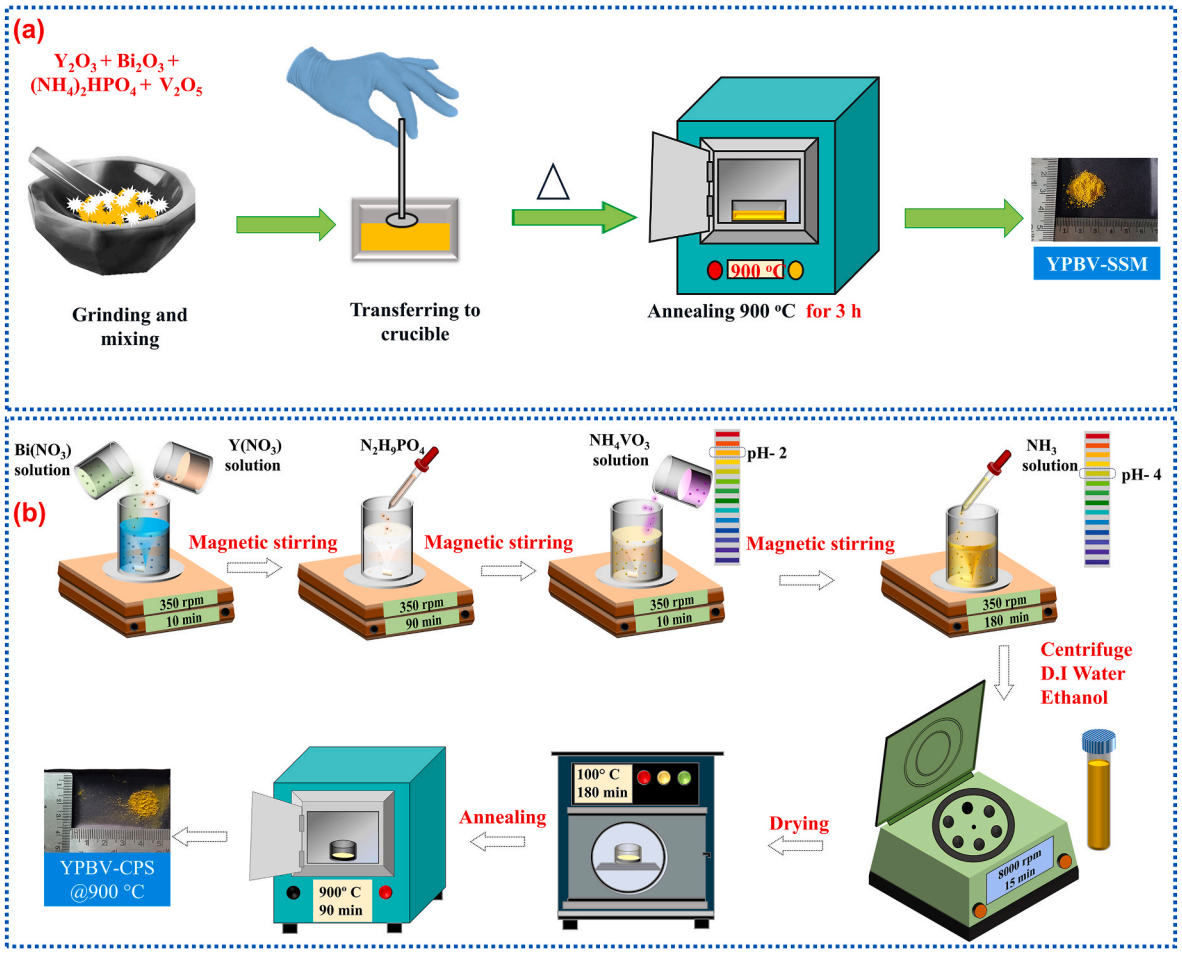

Fig. 1. Synthesis procedure of $Y_{(1-x)}Bi_xP_{(1-y)}V_yO_4$ (x = y = 0.6) material: (a) solid-state method (SSM), (b) co-precipitation method (CPS).

luminescent materials where rare-earth ion doping has been employed in the $YP_{1-x}V_xO_4$ (x = 0–1) lattice system [24,25]. These studies have concluded that lattice strain and peak shifts toward lower angles are primarily a result of V^{5+} substitution rather than rare-earth ion incorporation. This reinforces the idea that the structural modifications in the present study are predominantly driven by vanadium substitution effects rather than external dopant influences.

3.2. Thermogravimetric analysis (TGA)

The thermal stability and structural integrity of three representative materials were analyzed using thermogravimetric analysis (TGA) (see supplementary information (SI) Fig. S1). The weight loss profiles provided insights into the decomposition behavior and stability of the materials under elevated temperatures. For the YPBV-SSM sample, a minimal weight loss of approximately 0.2 % was observed below 400 °C, indicating negligible evaporation of adsorbed moisture or surface-bound volatiles. Similarly, the YPBV-CPS@900 °C sample exhibited a slightly higher weight loss of 0.4 % within the same temperature range. Beyond 400 °C, both materials displayed excellent thermal stability, with no significant weight loss up to 900 °C, confirming the absence of further decomposition or volatilization.

In contrast, the YPBV-CPS@100 °C sample exhibited a more substantial weight loss of 6.5 % below 300 °C, likely attributed to the removal of residual solvents, structural water, and loosely bound organic moieties. Upon further heating to 900 °C, an additional 1.5 % weight reduction was recorded, resulting in a total weight loss of 8.0 % over the entire thermal treatment range. This suggests a gradual release of thermally labile components [26]. Notably, beyond 900 °C, no further weight loss was detected in any of the materials, indicating complete stabilization. The superior thermal stability of YPBV-SSM and YPBV-CPS@900 °C compared to YPBV-CPS@100 °C can be attributed to the elimination of all volatile constituents during high-temperature processing, leading to a more structurally consolidated and thermally robust material.

3.3. Morphological and compositional analysis

SEM micrographs of $Y_{(1-x)}Bi_xP_{(1-y)}V_yO_4$ (x = y = 0.6) synthesized by the solid-state reaction and co-precipitation methods are illustrated in Fig. 3.

The SEM micrographs of $Y_{(1-x)}Bi_xP_{(1-y)}V_yO_4$ (x = y = 0.6) synthesized via the solid-state reaction and co-precipitation methods are presented in Fig. 3a–c. The images distinctly reveal that the particles exhibit significant aggregation, primarily due to the rapid nucleation and subsequent particle growth during the co-precipitation process, followed by high-temperature calcination at 900 °C. The aggregation of nanoparticles begins with the formation of pre-nuclei as the precursor materials dissolve in the reaction medium [27]. As nucleation progresses, new interfacial boundaries form between adjacent nuclei, facilitating nanoparticle growth due to the free energy supplied during synthesis. In certain cases, pre-nucleation clusters may form, promoting the aggregation of small particles. These aggregated structures exhibit strong interparticle interactions, making them highly stable and resistant to separation, even under mechanical milling [28].

The incorporation of vanadium (V^{5+}) and bismuth (Bi^{3+}) into the tetragonal YPO_4 lattice does not induce any significant morphological changes. However, high-temperature calcination at 900 °C plays a

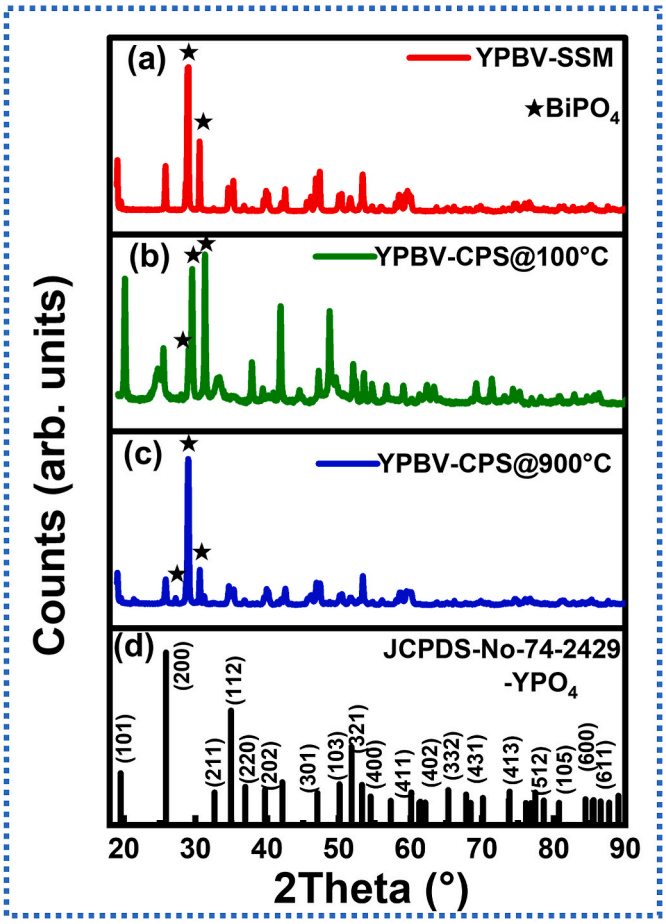

Fig. 2. PXRD pattern of ($Y_{(1-x)}$ Bi_x $P_{(1-y)}V_y$ O_4 ($x = y = 0.6$)) (a) YPBV-SSM, (b) YPBV-CPS@100 °C, (c) YPBV-CPS@900 °C, (d) YPO_4 (JCPDS-No-74-2429).

crucial role in modifying the particle morphology and size, as evident in Fig. 3c. The estimated average particle size from Fig. 3c is approximately 80 nm, which is in good agreement with the crystallite size determined from PXRD analysis. The irregularly shaped agglomerates are randomly oriented and exhibit remarkable thermal stability, showing negligible structural variations even at elevated temperatures up to 1100 °C [26]. Furthermore, energy-dispersive X-ray spectroscopy (EDAX) analysis confirms that the elemental composition closely matches the expected stoichiometric ratios of the constituent elements. The quantitative presence of Y, P, V, Bi, and O in the synthesized materials, as depicted in the inset tables, validates the successful incorporation of these elements into the material's crystalline framework.

3.4. FTIR analysis

The FTIR spectra of $Y_{(1-x)}Bi_xP_{(1-y)}V_yO_4$ ($x = y = 0.6$) synthesized via the solid-state reaction and co-precipitation methods are presented in Fig. 4a–c over the spectral range of 400–1500 cm^{-1}. These spectra provide valuable insights into the vibrational modes associated with the metal-oxide interactions in the synthesized materials, confirming the presence of Y, V, P, Bi, and O within the lattice structure. The characteristic absorption bands observed at 521, 594, 646, 733, 810, and 1021 cm^{-1} correspond to different vibrational modes of phosphate (PO_4^{3-}), vanadate (VO_4^{3-}), and metal-oxygen bonds. The absorption peak at 521 cm^{-1} is attributed to the bending vibration harmonics of the O=P=O bond. Prominent vibrational features at 594 and 646 cm^{-1}, observed consistently in all materials, are associated with the asymmetric stretching and distorted vibrational modes of the $(PO_4)^{3-}$ phosphate group. A distinct peak at 733 cm^{-1}, appearing in the spectra of YPBV-SSM and YPBV-CPS@900 °C, is indicative of the presence of pyrophosphate ($P_2O_7^{4-}$) groups, suggesting partial polymerization of phosphate units under high-temperature conditions [29]. The peak at 810 cm^{-1} corresponds to the P–O stretching vibrations, further affirming the structural integrity of the phosphate framework[30–32]. Additionally, an absorption band at 1021 cm^{-1} is observed in both YPBV-SSM and YPBV-CPS@900 °C, which is attributed to the presence of vanadate (VO_4^{3-}) groups, confirming the successful incorporation of vanadium into the phosphate lattice [33].

Furthermore, low-frequency vibrational modes in the range of 400–450 cm^1 correspond to metal-oxygen interactions, specifically Bi–O and Y–O bonds, which validate the structural stability of the doped yttrium phosphate matrix [34]. These findings are consistent with previous reports on rare-earth and vanadium-doped YPO_4 systems, where similar spectral features were observed. The collective spectral data confirms the successful synthesis of vanadium- and bismuth-doped

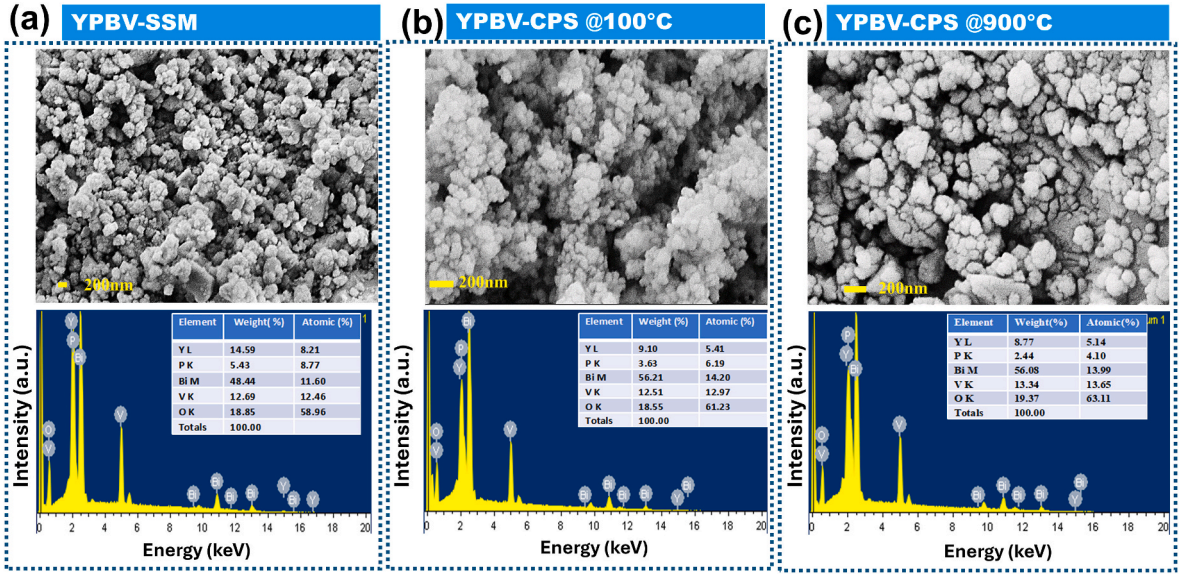

Fig. 3. SEM images and corresponding EDX spectra of $Y_{(1-x)}$ Bi_x $P_{(1-y)}V_y$ O_4 ($x = y = 0.6$) materials (a) YPBV-SSM, (b) YPBV-CPS@100 °C, (c) YPBV-CPS@900 °C. Inset tables represent the elemental composition of $Y_{(1-x)}$ Bi_x $P_{(1-y)}V_y$ O_4 ($x = y = 0.6$).

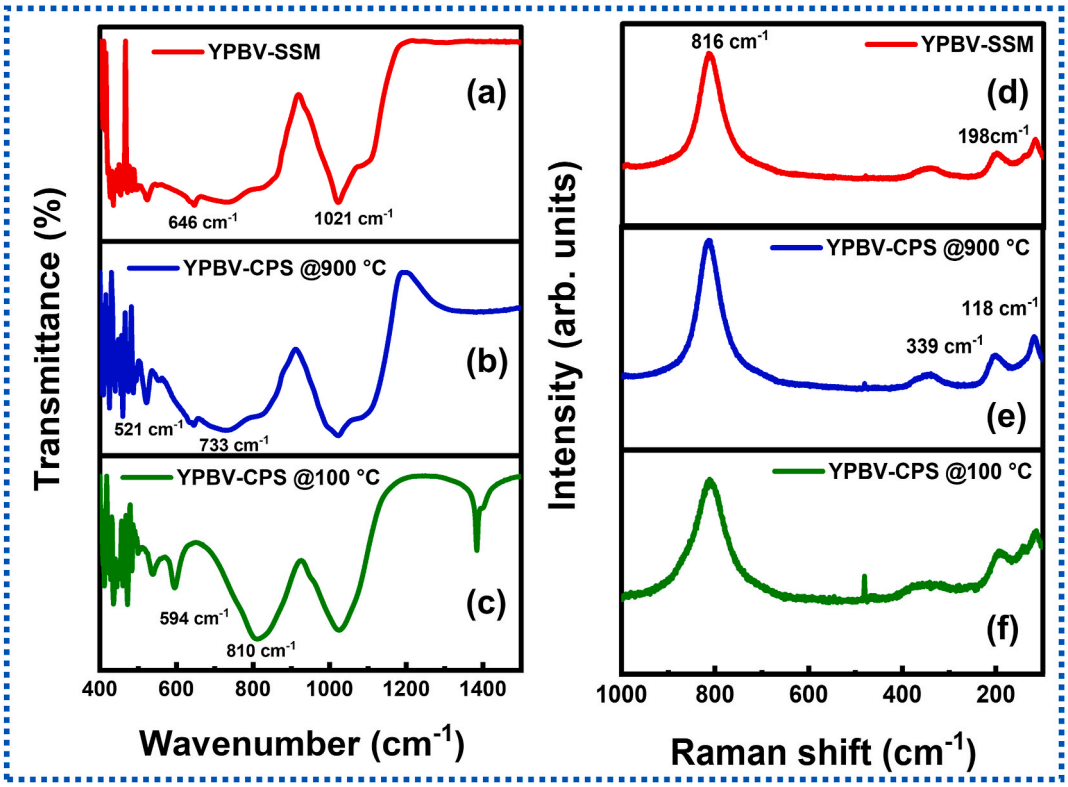

Fig. 4. (a) FTIR Spectra, and (b) Raman Spectra of $Y_{(1-x)}$ Bi_x $P_{(1-y)}V_y$ O_4 ($x = y = 0.6$) materials.

yttrium phosphate materials with well-defined structural integrity.

3.5. Raman Spectral analysis

The vibrational characteristics of synthesized $Y_{(1-x)}Bi_xP_{(1-y)}V_yO_4$ (x = y = 0.6) materials were analyzed using Raman spectroscopy within the frequency range of 200–1000 cm^{-1}, as illustrated in Fig. 4d-f. The recorded Raman spectra exhibit distinct vibrational modes corresponding to phosphate (PO_4^{3-}), vanadate (VO_4^{3-}), and Bi–O interactions, which provide crucial insights into the structural integrity and bonding environment of the synthesized materials [32].

All three materials exhibit similar Raman peaks, confirming the retention of the fundamental vibrational characteristics across different synthesis routes. Notably, the prominent Raman bands observed at 816, 339, 198, and 117 cm^{-1} correspond to the symmetric stretching vibrations of various molecular units within the lattice. The characteristic peak at 816 cm^{-1} is assigned to the symmetric stretching mode of the VO_4^{3-} tetrahedral units, which indicates the successful incorporation of vanadium into the phosphate framework [35]. The peak at 339 cm^{-1} is attributed to the bending vibrational mode of the PO_4^{3-} units, while the band observed at 198 cm^{-1} is associated with the O–Bi–O bending vibrations, further confirming the presence of bismuth in the system [36,37]. In addition to these dominant peaks, Raman shifts exceeding 1000 cm^{-1} (not depicted in Fig. 5) correspond to the asymmetric stretching vibrations of the PO_4^{3-} groups, which further validate the structural integrity of the phosphate network. The presence of these well-defined vibrational modes suggests strong metal-oxide interactions within the $Y_{(1-x)}Bi_xP_{(1-y)}V_yO_4$ system. The comprehensive Raman analysis confirms the coexistence of phosphate and vanadate moieties along with strong Bi–O bonding, reinforcing the stability and structural robustness of the synthesized materials.

3.6. UV-DRS analysis

Fig. 5a presents the UV–Vis diffuse reflectance spectra (UV-DRS) of $Y_{(1-x)}Bi_xP_{(1-y)}V_yO_4$ (x = y = 0.6) synthesized via the solid-state reaction and co-precipitation methods.

As previously reported, pure YPO_4 exhibits a weak absorption band between 230 and 330 nm, which is attributed to charge transfer transitions between the divalent oxygen ions (O^{2-}) and pentavalent phosphorus ions (P^{5+}). Consequently, YPO_4 appears white in color [38]. Upon the introduction of vanadium into the YPO_4 lattice, an additional absorption feature emerges in the range of 350–470 nm. This phenomenon is primarily ascribed to charge transfer transitions between V^{5+} and O^{2-} rather than d–d electronic transitions, given that V^{5+} possesses a d^0 electronic configuration [39]. The incorporation of vanadium leads to the development of a distinct yellow hue in the synthesized materials. With the co-substitution of bismuth and vanadium, a gradual redshift in the absorption edge is observed, ultimately reaching approximately 450 nm when 60 % of Y^{3+} and P^{5+} are replaced by Bi^{3+} and V^{5+}, respectively. Since 400–410 nm falls within the violet region of the visible spectrum, its complementary color (yellow) is prominently observed in the materials [40].

The observed spectral shift is attributed to the formation of vanadate (VO_4^{3-}) transitions in the phosphorous lattice. Additionally, hybrid orbital transitions occur due to the interaction between Bi 6s, O 2p, and V 3d orbitals, further contributing to the shift in absorption maxima. The UV-DRS spectra reveal that the materials synthesized via solid-state reaction (YPBV-SSM) and those calcined at 900 °C via co-precipitation (YPBV-CPS@900 °C) exhibit a more pronounced shift in absorption maxima toward longer wavelengths (~450 nm) compared to the sample synthesized at a lower calcination temperature (YPBV-CPS@100 °C), which shows an absorption maximum at approximately 300 nm in the UV region. This redshift in absorption correlates with the intensified yellow coloration observed in the bismuth- and vanadium-co-doped $Y_{(1-x)}Bi_xP_{(1-y)}V_yO_4$ materials.

As depicted in SI Figure S2, digital images of the synthesized materials confirm the progressive enhancement of the yellow hue with increasing Bi^{3+} and V^{5+} content [24,41]. Notably, materials calcined at higher temperatures (900 °C) exhibit a more vivid yellow color

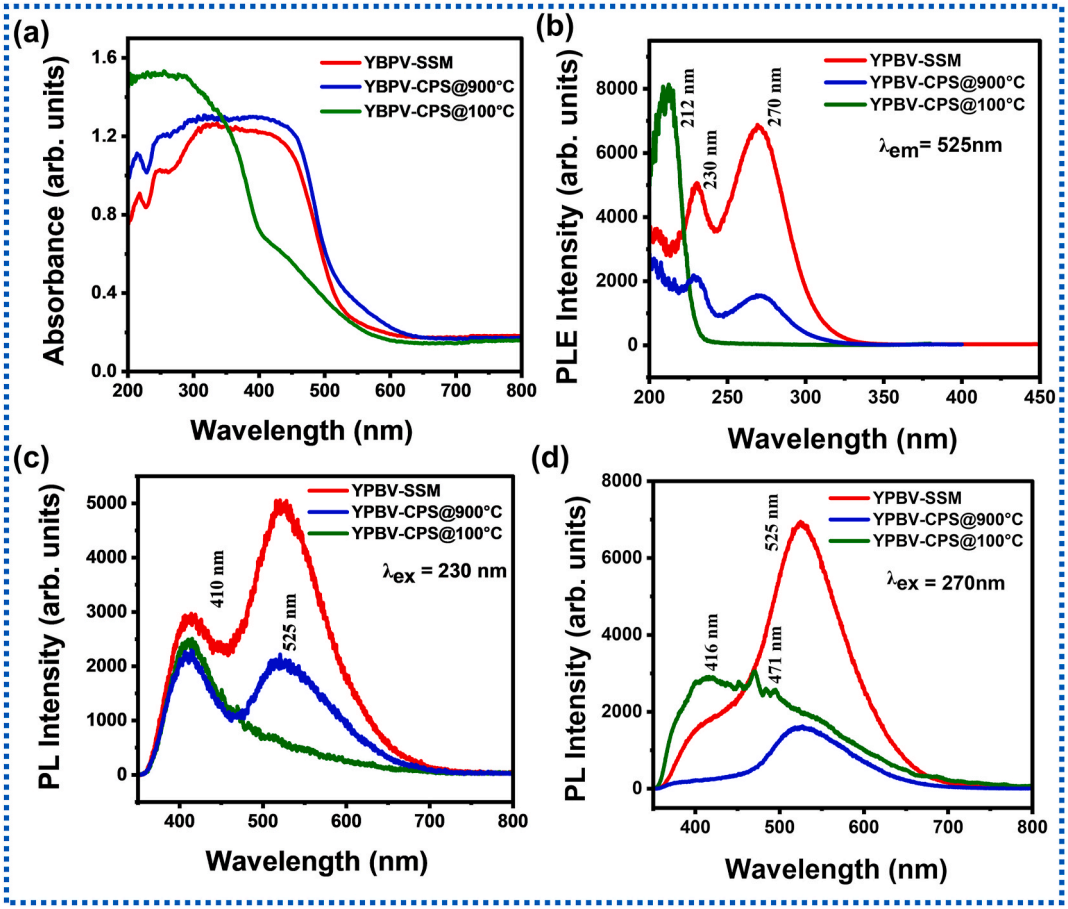

Fig. 5. (a) UV-DRS spectrum of $Y_{(1-x)}$ Bi_x $P_{(1-y)}V_y$ O_4 ($x = y = 0.6$) (b) PL excitation spectra of $Y_{(1-x)}$ Bi_x $P_{(1-y)}V_y$ O_4 ($x = y = 0.6$) recorded at 525 nm emission. PL spectra of $Y_{(1-x)}$ Bi_x $P_{(1-y)}V_y$ O_4 ($x = y = 0.6$) recorded at (c) 230 nm and (d) 270 nm excitations.

compared to those processed at lower temperatures (100 °C), indicating that thermal treatment influences chromatic properties by stabilizing the dopant-induced color centers.

The hue angle (h°), a key parameter in the CIELAB color space, quantifies the perceived color, with 90° corresponding to pure yellow. Materials with hue angles between 70° and 105° exhibit yellow hues, ranging from slightly greenish-yellow to reddish-yellow. Literature reports suggest that materials exhibiting a hue angle between 70° and 105° predominantly display a yellow appearance [42,43]. In the present study, all synthesized $Y_{(1-x)}Bi_xP_{(1-y)}V_yO_4$ (x = y = 0.6) materials fall within this hue angle range, further validating the development of a yellow body color as a result of Bi^{3+} and V^{5+} co-doping [44].

3.7. Photoluminescence studies

Fig. 5(b–d) represents the photoluminescence studies carried out on the synthesized $Y_{(1-x)}Bi_xP_{(1-y)}V_yO_4$ (x = y = 0.6) materials. The photoluminescence excitation (PLE) spectrum of $Y_{(1-x)}Bi_xP_{(1-y)}V_yO_4$ (x = y = 0.6) crystalline materials reveal three distinct peaks at 212 nm, 230 nm, and 270 nm, as shown in Fig. 5b when monitored under 525 nm emission. The excitation spectrum exhibits a broad absorption range extending from 210 to 400 nm, with prominent peaks centered at 230 nm and 270 nm, accompanied by a lower-intensity shoulder at 212 nm. Both the YPBV-SSM and YPBV-CPS@900 °C samples display similar excitation features, whereas the YPBV-CPS@100 °C sample exhibits a distinct excitation peak at 212 nm [45].

The presence of these peaks indicates efficient energy transfer processes and characteristic electronic transitions associated with both Bi^{3+} and V^{5+} ions in the YPO_4 host matrix. The peak at 212 nm can be attributed to the charge transfer transition from the O^{2-} ligands to the central V^{5+} ion within the VO_4^{3-} tetrahedral complex, which typically exhibits strong absorption in the deep UV region due to ligand-to-metal charge transfer transitions [46,47]. The 230 nm peak corresponds to the intra-configurational $6s^2 \rightarrow 6s,6p$ transition of Bi^{3+} ions, which is consistent with the allowed electric dipole transitions of Bi^{3+} in a crystalline environment with low site symmetry. The 270 nm peak likely arises from combined contributions of the $^1S_0 \rightarrow {}^3P_1$ transition of Bi^{3+} and the defect-related or crystal field-modified states of V^{5+} within the YPO_4 lattice [44]. The efficient energy transfer from V^{5+} to Bi^{3+} under UV excitation suggests a strong coupling between the Bi^{3+} and V^{5+} sites, facilitated by the rigid YPO_4 lattice, which enhances the overall luminescence intensity at 525 nm.

The photoluminescence emission (PL) spectrum of $Y_{(1-x)}Bi_xP_{(1-y)}V_yO_4$ (x = y = 0.6) crystalline materials exhibit distinct peaks at 525 nm and 410 nm when excited with 230 nm and 270 nm wavelengths, indicating efficient energy transfer and well-defined electronic transitions within the Bi^{3+} and V^{5+} co-doped YPO_4 lattice. Upon excitation at 230 nm, the 410 nm emission peak is attributed to the $^3P_1 \rightarrow {}^1S_0$ transition of Bi^{3+} ions, which arises from the relaxation of the electron from the excited 6s6p state to the ground $6s^2$ state. This transition is characteristic of Bi^{3+} in a low-symmetry crystalline environment, where the parity-forbidden nature of the transition is relaxed due to crystal field effects, leading to enhanced luminescence. The emission at 525 nm upon 270 nm excitation is associated with the involvement of V^{5+} ions, where the energy transfer from the V^{5+}-associated VO_4^{3-} tetrahedra to Bi^{3+} ions enable green (525 nm) emission. The 525 nm peak corresponds to the interaction of Bi^{3+}-based electronic states modified by the crystal field and coupling with V^{5+} states, suggesting an

efficient energy transfer pathway from V^{5+} to Bi^{3+}. The presence of these distinct emissions highlights the role of the YPO_4 host lattice in stabilizing the dopant ions and facilitating energy/heat migration, making Bi^{3+} and V^{5+} co-doped YPO_4 a promising candidate for cool-coating applications [24,25].

3.8. Estimation of quantum yield from reflectance spectra

Fig. 6a represents reflectance spectra of $Y_{(1-x)}Bi_xP_{(1-y)}V_yO_4$ (x = y = 0.6) materials in the UV–Vis–NIR range.

The quantum yield (QY) estimation of Bi^{3+} and V^{5+} co-doped YPO_4 crystalline materials from reflectance spectra in the UV–Visible–NIR range (300–1000 nm) involves several analytical steps. The diffuse reflectance spectrum (DRS) is initially recorded using an integrating sphere to capture the total reflected light, including both specular and diffuse components. The reflectance data are then converted into the corresponding absorption spectrum using the Kubelka-Munk (KM) function, $F(R) = (1\text{-}R)^2/2R$, where R is the absolute reflectance [48]. This transformation provides an estimate of the absorption coefficient, crucial for analyzing the energy absorption characteristics of the material. The absorption and emission profiles are subsequently correlated to determine the internal quantum efficiency (IQE), which is given by the ratio of the number of emitted photons to the number of absorbed photons. The PL spectrum is obtained under UV excitation, typically at the excitation wavelength corresponding to the maximum absorption band, which in this case is influenced by the charge transfer transitions between Bi^{3+}-O^{2-} and V^{5+}-O^{2-} rather than d-d transitions, as V^{5+} has a d^0 electronic configuration. The external quantum yield (EQY) is then calculated using the relation $EQY = \frac{I_{em}}{Iex} X\ 100\%$, where I_{em} is the integrated emission intensity and I_{ex} is the total incident excitation intensity [49]. To refine the estimation, a standard phosphor with a known quantum yield, such as YAG: Ce^{3+}, is used as a reference to normalize the spectral response and account for instrumental factors. The presence of Bi^{3+} and V^{5+} dopants enhance light absorption in the near-UV and visible regions, facilitating energy transfer and modifying the radiative recombination pathways, thereby affecting quantum efficiency. Additionally, integrating sphere measurements can be employed to directly measure absolute quantum yield by capturing the total emission relative to absorbed excitation light. A significant red shift in absorption, due to Bi^{3+} and V^{5+} co-substitution in the YPO_4 lattice, indicates bandgap modulation, which directly impacts quantum yield by altering the recombination dynamics and radiative efficiency of the system [49,50].

3.9. NIR solar reflectance spectral analysis

Fig. 6b represents NIR solar reflectance spectra of $Y_{(1-x)}Bi_xP_{(1-y)}V_yO_4$ (x = y = 0.6) materials in the NIR range [50]. The samples synthesized via the solid-state reaction (YPBV-SSM) and co-precipitation, followed by high-temperature calcination at 900 °C (YPBV-CPS@900 °C) exhibited average NIR solar reflectance values of 54.64 % and 51.54 %, respectively. In contrast, the sample synthesized via co-precipitation and heat-treated at 100 °C (YPBV-CPS@100 °C) displayed irregular and inconsistent reflectance across the entire NIR spectral range of 800–2400 nm. A substantial increase in NIR solar reflectance was observed in two specific cases: (1) when both Bi^{3+} and V^{5+} ions were simultaneously doped into the YPO_4 lattice and (2) when the YPBV-CPS@100 °C sample was subjected to calcination at 900 °C for 3 h. Under these conditions, the NIR solar reflectance values approached 54.64 % for $Y_{0.4}Bi_{0.6}P_{0.4}V_{0.6}O_4$, demonstrating the impact of both co-doping and thermal treatment on optical properties [51].

The enhancement in reflectance is primarily attributed to morphological changes induced by Bi^{3+} and V^{5+} co-doping in the YPO_4 crystal structure. According to KM theory, the scattering coefficient (S) is inversely proportional to the mean particle size (d). When the particle size is reduced to below 1 μm, the scattering efficiency of the material increases, thereby enhancing reflectance. In this study, the co-doped sample ($Y_{0.4}Bi_{0.6}P_{0.4}V_{0.6}O_4$) exhibited the smallest mean particle size of 98 nm, which was notably lower than that of vanadium-only substituted YPO_4 materials. Additionally, KM theory suggests that well-defined particle morphology and uniform distribution further contribute to high NIR solar reflectance. The superior reflectance observed in the YPBV-SSM sample compared to the YPBV-CPS@900 °C sample can be attributed to its more regular particle shape and uniform dispersion. This finding aligns with previous studies, where researchers have reported that materials composed of uniformly distributed, well-shaped spherical particles with minimal agglomeration exhibit enhanced NIR reflectance.

4. Conclusions

A new class of environmentally sustainable yellow pigments with superior near-infrared (NIR) solar reflectance has been engineered by dual substitution of bismuth (Bi^{3+}) and vanadium (V^{5+}) into the yttrium phosphate (YPO_4) framework. A systematic series of $Y_{(1-x)}Bi_xP_{(1-y)}V_yO_4$ (x = y = 0–1) compositions were synthesized via flux-assisted solid-state reaction and co-precipitation methods, allowing for a comparative analysis of their optical and structural properties. A significant redshift in the absorption spectrum was observed for materials prepared using the solid-state reaction method and co-precipitation followed by high-temperature calcination at 900 °C. The presence of secondary phases in both synthesis routes was attributed to the large ionic radii of the dopant ions. Notably, the simultaneous incorporation of Bi^{3+} and V^{5+}

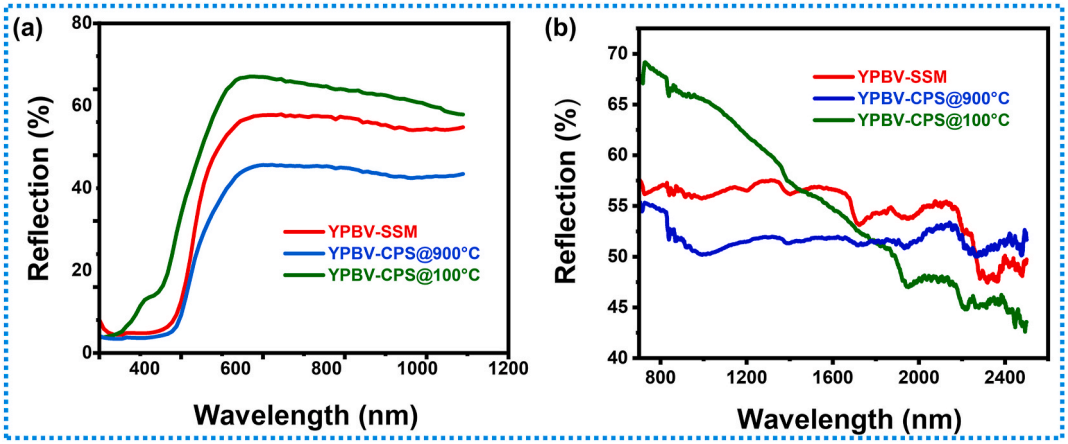

Fig. 6. (a) Reflectance spectra of $Y_{(1-x)}$ Bi_x $P_{(1-y)}V_y$ O_4($x = y = 0.6$) in the UV–Visible–NIR range, (b) NIR solar reflectance spectra of $Y_{(1-x)}$ Bi_x $P_{(1-y)}V_y$ O_4 ($x = y =$ 0.6) materials in the NIR range.

resulted in a remarkable enhancement in both NIR solar reflectance and the intensity of the yellow coloration. This co-doping strategy also promoted a well-defined morphological features, improving light-scattering efficiency and elevating the NIR solar reflectance from 38 % for pristine YPO_4 to an impressive 54.64 % for $Y_{0.4}Bi_{0.6}P_{0.4}V_{0.6}O_4$, while maintaining excellent durability and color stability. With its yellow appearance, superior solar reflectance (54.64 %), and outstanding thermal and environmental stability, $Y_{0.4}Bi_{0.6}P_{0.4}V_{0.6}O_4$ emerges as a highly promising, sustainable alternative for next-generation cool yellow pigments in energy-efficient coatings, architectural applications, and urban heat mitigation strategies.

CRediT authorship contribution statement

A. Mridula: Writing – original draft, Methodology, Investigation, Formal analysis, Data curation. **M. Rakshita:** Methodology, Formal analysis, Data curation. **K.A.K. Durga Prasad:** Methodology, Formal analysis, Data curation. **Subrata Das:** Methodology, Formal analysis, Data curation. **K. Uday Kumar:** Writing – review & editing, Writing – original draft, Supervision, Methodology, Funding acquisition, Conceptualization. **S. Surendra Babu:** Methodology, Funding acquisition, Formal analysis, Conceptualization. **R. Rakesh Kumar:** Writing – review & editing, Formal analysis. **D. Haranath:** Writing – review & editing, Supervision, Methodology, Funding acquisition, Conceptualization.

Declaration of competing interest

The authors declare that they have no known competing financial interests or personal relationships that could have appeared to influence the work reported in this paper.

Appendix A. Supplementary data

Supplementary data to this article can be found online at https://doi.org/10.1016/j.mssp.2025.109755.

Data availability

Data will be made available on request.

References

[1] Q. Li, H. Zhang, X. Liu, J. Huang, Urban heat island effect on annual mean temperature during the last 50 years in China, Theor. Appl. Climatol. 79 (2004) 165–174, https://doi.org/10.1007/s00704-004-0065-4.

[2] K.J. Chua, S.K. Chou, W.M. Yang, J. Yan, Achieving better energy-efficient air conditioning – a review of technologies and strategies, Appl. Energy 104 (2013) 87–104, https://doi.org/10.1016/J.APENERGY.2012.10.037.

[3] S. Bretz, H. Akbari, A. Rosenfeld, Practical issues for using solar-reflective materials to mitigate urban heat islands, Atmos. Environ. 32 (1998) 95–101, https://doi.org/10.1016/S1352-2310(97)00182-9.

[4] Z. Xu, D. Wang, M. Zhong, Z. Zhang, Preparation and characterization of Mg2+-doped CaCu3Ti4O12 pigment with high NIR reflectance, Ceram. Int. 46 (2020) 25306–25312, https://doi.org/10.1016/J.CERAMINT.2020.06.324.

[5] Y. Zhang, Y. Zhang, X. Zhao, Y. Zhang, Sol–gel synthesis and properties of europium–strontium copper silicates blue pigments with high near-infrared reflectance, Dyes Pigments 131 (2016) 154–159, https://doi.org/10.1016/J.DYEPIG.2016.04.011.

[6] J. Janicki, R. Troc, Quasi-one-dimensional magnetic properties of the (In;Sc;Lu;Y) 2Cu2O5 oxides, J. Phys. Condens. Matter 4 (1992) 6267, https://doi.org/10.1088/0953-8984/4/29/010.

[7] C. Ding, A. Han, M. Ye, Y. Zhang, L. Yao, J. Yang, Hydrothermal synthesis and characterization of novel yellow pigments based on V5+ doped BiPO4 with high near-infrared reflectance, RSC Adv. 8 (2018) 19690–19700, https://doi.org/10.1039/C8RA02406E.

[8] Y. Yuan, Y. Wu, N. Suganthy, S. Shanmugam, K. Brindhadevi, A. Sabour, M. Alshiekheid, N.T. Lan Chi, A. Pugazhendhi, R. Shanmuganathan, Biosynthesis of zirconium nanoparticles (ZrO2 NPs) by Phyllanthus niruri extract: characterization and its photocatalytic dye degradation activity, Food Chem. Toxicol. 168 (2022) 113340, https://doi.org/10.1016/J.FCT.2022.113340.

[9] B. Gopal, A. Muralidharan, R. Bakthavatsalam, S. Nellaiappan, A. Senthil Kumar, Unusual observation of optical property of V5+ substituted BPO4 and its tunable redox features, Mater. Res. Bull. 91 (2017) 122–126, https://doi.org/10.1016/J.MATERRESBULL.2017.03.020.

[10] H. Lai, Y. Du, M. Zhao, K. Sun, L. Yang, CTAB assisted hydrothermal preparation of YPO4:Tb3+ with controlled morphology, structure and enhanced photoluminescence, Mater. Sci. Eng., B 179 (2014) 66–70, https://doi.org/10.1016/J.MSEB.2013.10.007.

[11] Y. Zhang, Z. Yan, L. You, R. Si, C. Yan, General synthesis and characterization of monocrystalline lanthanide orthophosphate nanowires, Eur. J. Inorg. Chem. 2003 (2003) 4099–4104, https://doi.org/10.1002/ejic.200300399.

[12] Z.-G. Yan, Y.-W. Zhang, L.-P. You, R. Si, C.-H. Yan, General synthesis and characterization of monocrystalline 1D-nanomaterials of hexagonal and orthorhombic lanthanide orthophosphate hydrate, J. Cryst. Growth 262 (2004) 408–414, https://doi.org/10.1016/j.jcrysgro.2003.10.058.

[13] P. Ghosh, E. de la Rosa, J. Oliva, D. Solis, A. Kar, A. Patra, Influence of surface coating on the upconversion emission properties of LaPO4:Yb/Tm core-shell nanorods, J. Appl. Phys. 105 (2009) 113532, https://doi.org/10.1063/1.3143890.

[14] C.G. Ma, A.V. Popov, A.S. Vanetsev, O.M. Gaitko, E.O. Orlovskaya, S. Lange, I. Sildos, Y.V. Orlovskii, Vacuum ultraviolet spectroscopic analysis of Ce3+-doped hexagonal YPO4·0.8H2O based on exchange charge model, J. Lumin. 152 (2014) 70–74, https://doi.org/10.1016/j.jlumin.2013.10.069.

[15] A.S. Vanetsev, E.V. Samsonova, O.M. Gaitko, K. Keevend, A.V. Popov, U. Mäeorg, H. Mändar, I. Sildos, YuV. Orlovskii, Phase composition and morphology of nanoparticles of yttrium orthophosphates synthesized by microwave-hydrothermal treatment: the influence of synthetic conditions, J. Alloys Compd. 639 (2015) 415–421, https://doi.org/10.1016/j.jallcom.2015.03.125.

[16] Kh Chanchan, S.D. Singh, Concentration effect on the luminescent and structural properties of YPO4: Eu3+, Mater. Today Proc. 65 (2022) 2480–2483, https://doi.org/10.1016/j.matpr.2022.04.055.

[17] I.S. Pruthviraj, B.R.R. Krushna, S.C. Sharma, H.B. Premkumar, K. Manjunatha, S. Y. Wu, S. Mishra, L. Ganesan, D.G. Kumar, A. George, J.B.P. Kumar, H. Nagabhushana, Synergistic Ce3+, Tb3+ activated LaCaAl3O7 phosphor: bridging forensic science with advanced w-LEDs applications, J. Lumin. 280 (2025) 121080, https://doi.org/10.1016/j.jlumin.2025.121080.

[18] L. Sun, B. Devakumar, J. Liang, S. Wang, Q. Sun, X. Huang, Highly efficient Ce $^{3+}$ → Tb $^{3+}$ energy transfer induced bright narrowband green emissions from garnet-type Ca $_2$ YZr $_2$ (AlO $_4$) $_3$:Ce $^{3+}$,Tb $^{3+}$ phosphors for white LEDs with high color rendering index, J Mater Chem C Mater 7 (2019) 10471–10480, https://doi.org/10.1039/C9TC03664D.

[19] F. Angiuli, E. Cavalli, P. Boutinaud, R. Mahiou, Emission properties of Sm3+/Bi3+-doped YPO4 phosphors, J. Lumin. 135 (2013) 239–242, https://doi.org/10.1016/j.jlumin.2012.10.005.

[20] M. Wujczyk, A. Watras, K. Szyszka, R.J. Wiglusz, Influence of vanadium concentration on up-conversion luminescence in Er3+–Yb3+ and Tm3+–Yb3+ ions pair co-doped YVxP1−xO4 solid state solution, J. Alloys Compd. 884 (2021) 161022, https://doi.org/10.1016/J.JALLCOM.2021.161022.

[21] N. Abid, A.M. Khan, S. Shujait, K. Chaudhary, M. Ikram, M. Imran, J. Haider, M. Khan, Q. Khan, M. Maqbool, Synthesis of nanomaterials using various top-down and bottom-up approaches, influencing factors, advantages, and disadvantages: a review, Adv. Colloid Interface Sci. 300 (2022) 102597, https://doi.org/10.1016/J.CIS.2021.102597.

[22] H. Fang, X. Wei, S. Zhou, X. Li, Y. Chen, C.-K. Duan, M. Yin, Terbium and holmium codoped yttrium phosphate as non-contact optical temperature sensors, RSC Adv. 7 (2017) 10200–10205, https://doi.org/10.1039/C6RA27971F.

[23] Z. Xu, Q. Zhu, X. Li, X. Sun, J.-G. Li, White-light emitting (Y,Gd)PO4:Dy3+ microspheres: Gd3+ mediated morphology tailoring and selective energy transfer and correlation of photoluminescence behaviors, Mater. Res. Bull. 110 (2019) 149–158, https://doi.org/10.1016/j.materresbull.2018.10.032.

[24] E. Cavalli, F. Angiuli, F. Mezzadri, M. Trevisani, M. Bettinelli, P. Boutinaud, M. G. Brik, Tunable luminescence of Bi3+-doped YPxV1 − xO4 ($0 \leq x \leq 1$), J. Phys. Condens. Matter 26 (2014) 385503, https://doi.org/10.1088/0953-8984/26/38/385503.

[25] J. Sun, J. Xian, Z. Xia, H. Du, Synthesis, structure and luminescence properties of Y (V,P)O4:Eu3+,Bi3+ phosphors, J. Lumin. 130 (2010) 1818–1824, https://doi.org/10.1016/j.jlumin.2010.04.016.

[26] W. Di, X. Zhao, S. Lu, X. Wang, H. Zhao, Thermal and photoluminescence properties of hydrated YPO4:Eu3+ nanowires, J. Solid State Chem. 180 (2007) 2478–2484, https://doi.org/10.1016/j.jssc.2007.06.025.

[27] D. Li, R.B. Kaner, How nucleation affects the aggregation of nanoparticles, J. Mater. Chem. 17 (2007) 2279–2282, https://doi.org/10.1039/B700699C.

[28] P. Anantha Rao, V. Raghavendra, B. Suryanarayana, T. Paulos, N. Murali, P.V.S. K. Phanidhar Varma, R. Giri Prasad, Y. Ramakrishna, K. Chandramouli, Cadmium substitution effect on structural, electrical and magnetic properties of Ni-Zn nano ferrites, Results Phys. 19 (2020) 103487, https://doi.org/10.1016/j.rinp.2020.103487.

[29] E.M. Bouabdalli, M. El Jouad, S. Touhtouh, A. Hajjaji, First examination of the influence of Y3+ ions on the structural, physical and optical properties of strontium phosphate glasses, Opt Quantum Electron 55 (2023) 1–25, https://doi.org/10.1007/S11082-023-05075-2/METRICS.

[30] R. Kijkowska, E. Cholewka, B. Duszak, X-ray diffraction and Ir-absorption characteristics of lanthanide orthophosphates obtained by crystallisation from phosphoric acid solution, J. Mater. Sci. 38 (2003) 223–228, https://doi.org/10.1023/A:1021188810349.

[31] J.C. Batista, P.C. de Sousa Filho, O.A. Serra, Effect of the vanadium(v) concentration on the spectroscopic properties of nanosized europium-doped yttrium phosphates, Dalton Trans. (2003) 41 (2012) 6310–6318, https://doi.org/10.1039/C2DT30380A.

[32] K. Nakamoto, Theory of normal vibrations, infrared and Raman spectra of inorganic and coordination compounds, 1–147, https://doi.org/10.1002/9780470405840.CH1, 2008.
[33] M. Rakshita, A.A. Sharma, P.P. Pradhan, K.A.K.D. Prasad, M. Srinivas, D. Haranath, Fabrication and characterization of rare earth-free nanophosphor based devices for solid-state lighting applications, Mater. Adv. (2025), https://doi.org/10.1039/D5MA00117J.
[34] M.N. Luwang, R.S. Ningthoujam, S.K. Srivastava, R.K. Vatsa, Disappearance and recovery of luminescence in Bi3+, Eu3+ codoped YPO4 nanoparticles due to the presence of water molecules up to 800 °C, J. Am. Chem. Soc. 133 (2011) 2998–3004, https://doi.org/10.1021/ja1092437.
[35] I.E. Kolesnikov, A.A. Kalinichev, M.A. Kurochkin, E. V Golyeva, A.S. Terentyeva, E. Yu Kolesnikov, E. Lähderanta, Structural, luminescence and thermometric properties of nanocrystalline YVO4:Dy3+ temperature and concentration series, Sci. Rep. 9 (2019) 2043, https://doi.org/10.1038/s41598-019-38774-6.
[36] A.B. Azzam, S.M. El-Sheikh, R.A. Geioushy, B.A. Salah, F.M. El-Dars, A.S. Helal, Facile fabrication of a novel BiPO4 phase junction with enhanced photocatalytic performance towards aniline blue degradation, RSC Adv. 9 (2019) 17246–17253, https://doi.org/10.1039/C9RA02315A.
[37] A. Bouddouch, E. Amaterz, B. Bakiz, F. Guinneton, A. Taoufyq, S. Villain, J.-R. Gavarri, M. Mansori, J.-C. Valmalette, A. Benlhachemi, High photocatalytic performance of bismuth phosphate and corresponding photodegradation mechanism of Rhodamine B, Res. Chem. Intermed. 48 (2022) 3315–3334, https://doi.org/10.1007/s11164-022-04762-1.
[38] S. Sameera, P. Prabhakar Rao, V. James, S. Divya, A.K. V Raj, Influence of (LiLa)1/2MoO4 substitution on the pigmentary properties of BiVO4, Dyes Pigments 104 (2014) 41–47, https://doi.org/10.1016/j.dyepig.2013.12.029.
[39] J. Wu, H. Jia, M. Li, H. Jia, Z. Liu, Influence of pH on nano-phosphor YPO4:2%Sm3+ and luminescent properties, Appl. Phys. A 126 (2020) 87, https://doi.org/10.1007/s00339-019-3257-6.
[40] S. Sameera, P. Prabhakar Rao, V. James, S. Divya, A.K.V. Raj, Influence of (LiLa)1/2MoO4 substitution on the pigmentary properties of BiVO4, Dyes Pigments 104 (2014) 41–47, https://doi.org/10.1016/J.DYEPIG.2013.12.029.
[41] C. Ding, A. Han, M. Ye, Y. Zhang, L. Yao, J. Yang, Hydrothermal synthesis and characterization of novel yellow pigments based on V5+ doped BiPO4 with high near-infrared reflectance, RSC Adv. 8 (2018) 19690–19700, https://doi.org/10.1039/C8RA02406E.
[42] R. Pandiselvam, S. Mitharwal, P. Rani, M.A. Shanker, A. Kumar, R. Aslam, Y. T. Barut, A. Kothakota, S. Rustagi, D. Bhati, S.A. Siddiqui, M.W. Siddiqui, S. Ramniwas, A. Aliyeva, A. Mousavi Khaneghah, The influence of non-thermal technologies on color pigments of food materials: an updated review, Curr. Res. Food Sci. 6 (2023) 100529, https://doi.org/10.1016/J.CRFS.2023.100529.
[43] M. Fedel, A. Rosati, S. Rossi, M. Picollo, F. Parrino, Environmentally friendly YIn0.9Fe0.1O3-ZnO yellow pigment displaying near infra red (NIR) reflectance and photocatalytic activity, Ceram. Int. 50 (2024) 15952–15964, https://doi.org/10.1016/J.CERAMINT.2024.02.075.
[44] V. Elakkiya, S. Sumathi, Bismuth and vanadium-substituted yttrium phosphates for cool coating applications, ACS Omega 7 (2022) 44266–44277, https://doi.org/10.1021/acsomega.2c05748.
[45] S. Ye, F. Xiao, Y.X. Pan, Y.Y. Ma, Q.Y. Zhang, Phosphors in phosphor-converted white light-emitting diodes: recent advances in materials, techniques and properties, Mater. Sci. Eng. R Rep. 71 (2010) 1–34, https://doi.org/10.1016/j.mser.2010.07.001.
[46] D.P.B. Vinuta, Y.S. Vidya, H.C. Manjunatha, S. Manjunatha, R. Munirathnam, M. Shivanna, S. Kumar, Electrochemical and photoluminescence properties of Zinc vanadate nanoparticles synthesized via chemical and green mediated route, Mater. Sci. Eng., B 306 (2024) 117449, https://doi.org/10.1016/J.MSEB.2024.117449.
[47] V. Chauhan, P. Deshmukh, S. Satapathy, P.C. Pandey, Greenish-yellow emission from rare-earth free Li+ doped zinc vanadate phosphor, Results Phys. 39 (2022) 105689, https://doi.org/10.1016/J.RINP.2022.105689.
[48] G. Maharana, R. Muniramaiah, J. Yuvashree, D. Mandal, S. Mondal, M. Kovendhan, J.M. Fernandes, G. Laxminarayana, D.P. Joseph, Tungsten and fluorine co-doping induced morphology change and textured growth of spray-pyrolyzed SnO2 thin films viable for photocatalytic application, Surf. Interfaces 42 (2023) 103413, https://doi.org/10.1016/j.surfin.2023.103413.
[49] Y. Piekner, D.S. Ellis, M. Schleuning, D.A. Grave, P. Schnell, H. Dotan, F.F. Abdi, A. Rothschild, External quantum efficiency spectra of BiVO 4 thin film photoanodes under bias illumination, J. Electrochem. Soc. 169 (2022) 046513, https://doi.org/10.1149/1945-7111/ac63f7.
[50] I.E. Kolesnikov, A.A. Kalinichev, M.A. Kurochkin, E. V Golyeva, E.Yu Kolesnikov, A. V Kurochkin, E. Lähderanta, M.D. Mikhailov, YVO4:Nd3+ nanophosphors as NIR-to-NIR thermal sensors in wide temperature range, Sci. Rep. 7 (2017) 18002, https://doi.org/10.1038/s41598-017-18295-w.
[51] Z. Tao, W. Zhang, Y. Huang, D. Wei, H.J. Seo, A novel pyrophosphate BaCr2(P2O7)2 as green pigment with high NIR solar reflectance and durable chemical stability, Solid State Sci. 34 (2014) 78–84, https://doi.org/10.1016/J.SOLIDSTATESCIENCES.2014.05.016.